



**HAL**  
open science

## Electron microscopy by specimen design: application to strain measurements

Nikolay Cherkashin, Thibaud Denneulin, Martin Hÿtch

► **To cite this version:**

Nikolay Cherkashin, Thibaud Denneulin, Martin Hÿtch. Electron microscopy by specimen design: application to strain measurements. *Scientific Reports*, 2017, 7 (1), pp.12394 - 12394. 10.1038/s41598-017-12695-8 . hal-01707848

**HAL Id: hal-01707848**

**<https://hal.science/hal-01707848>**

Submitted on 13 Feb 2018

**HAL** is a multi-disciplinary open access archive for the deposit and dissemination of scientific research documents, whether they are published or not. The documents may come from teaching and research institutions in France or abroad, or from public or private research centers.

L'archive ouverte pluridisciplinaire **HAL**, est destinée au dépôt et à la diffusion de documents scientifiques de niveau recherche, publiés ou non, émanant des établissements d'enseignement et de recherche français ou étrangers, des laboratoires publics ou privés.

# SCIENTIFIC REPORTS



OPEN

## Electron microscopy by specimen design: application to strain measurements

Nikolay Cherkashin, Thibaud Denneulin & Martin J. Hÿtch

**A bewildering number of techniques have been developed for transmission electron microscopy (TEM), involving the use of ever more complex combinations of lens configurations, apertures and detector geometries. In parallel, the developments in the field of ion beam instruments have modernized sample preparation and enabled the preparation of various types of materials. However, the desired final specimen geometry is always almost the same: a thin foil of uniform thickness. Here we will show that judicious design of specimen geometry can make all the difference and that experiments can be carried out on the most basic electron microscope and in the usual imaging modes. We propose two sample preparation methods that allow the formation of controlled moiré patterns for general monocrystalline structures in cross-section and at specific sites. We developed moiré image treatment algorithms using an absolute correction of projection lens distortions of a TEM that allows strain measurements and mapping with a nanometer resolution and  $10^{-4}$  precision. Imaging and diffraction techniques in other fields may in turn benefit from this technique in perspective.**

Developments in transmission electron microscopy (TEM) have centered on improving instrumentation and optical configurations. Considerable effort has also been put into developing sophisticated specimen preparation methods and equipment, from the humble ion-beam polisher, through tripod polishing and ultramicrotomy, to multifunction focused-ion beam (FIB) systems. However, the desired final specimen geometry is always the same: a thin foil of uniform thickness. Here we will show that judicious design of specimen geometry can make all the difference and that experiments can be carried out on the most basic electron microscope and in the usual imaging modes.

The example we have chosen to illustrate electron microscopy by specimen design is the measurement of strain in thin-films and devices. Strain engineering is now an important feature of many research areas, from strained-silicon transistors<sup>1</sup> to ferroelectrics<sup>2</sup> and thermoelectric materials<sup>3</sup>. It is therefore not surprising that many TEM techniques have been developed over the years to measure it accurately<sup>4</sup>. These include quantitative analysis of high-resolution transmission electron microscope images (HRTEM)<sup>5–7</sup>, convergent-beam electron diffraction (CBED)<sup>8</sup>, nano-beam electron diffraction (NBED)<sup>9,10</sup>, dark-field off-axis electron holography (DFEH)<sup>11</sup>, dark-field inline holography (DIH)<sup>12,13</sup> and more recently STEM moiré fringes (SMF)<sup>14,15</sup>.

All these techniques have specific instrumental requirements such as aberration correctors, Lorentz lenses or electrostatic biprisms (for holography). Even DIH and CBED require an imaging energy filter faced with the complexity of the data simulation and interpretation<sup>12,13,16,17</sup>. Our aim is not to belittle instrumental developments but to explore an alternative route to making measurements with electron microscopy that can, in some ways, be superior to existing techniques. How then can we design the specimen geometry to perform the technique on the most basic conventional TEM: by returning to the moiré imaging phenomenon known from the very beginnings of electron microscopy<sup>18,19</sup>.

Moiré patterns are a general interference phenomena that appear when two periodic arrays are superposed<sup>20</sup>. In TEM, they usually occur by chance, when two crystals with slightly different lattice parameters or orientation are superposed along the path of the electron beam (Fig. 1). In a bright-field (BF) image, the fringe pattern results from the interference of the transmitted beam passing through the two crystals with a doubly diffracted beam in crystal II. In a dark-field (DF) image, the resulting Moiré pattern arises from an interference between two beams diffracted in crystal I and II. Moiré fringes are formed if there is a vector difference  $\mathbf{m} = \mathbf{g}_2 - \mathbf{g}_1$  between the diffraction vectors I,  $\mathbf{g}_1$  and II,  $\mathbf{g}_2$ . The moiré spacing,  $m$ , can therefore be linked to the strain, or orientation

CEMES, CNRS, 29 rue Jeanne Marvig, 31055 TOULOUSE, Cedex 4, France. Correspondence and requests for materials should be addressed to N.C. (email: [nikolay.cherkashin@cemes.fr](mailto:nikolay.cherkashin@cemes.fr))

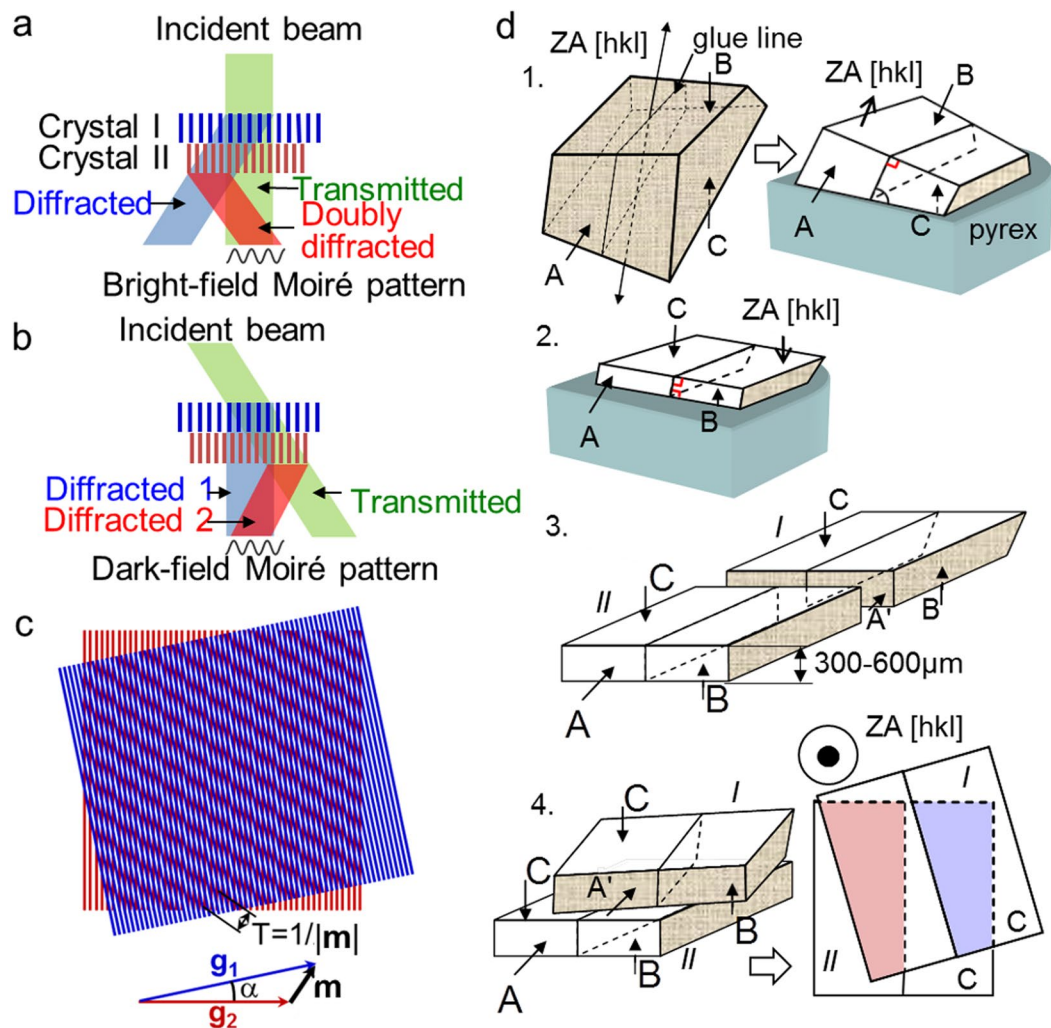


**Figure 1.** Formation of moiré fringes: two superimposed crystals with slightly different lattice parameters and rotated by an angle,  $\alpha$ , around the axis of the electron beam create interference: (a) In bright-field, between transmitted beam and a doubly diffracted beam. (b) In dark-field, between two diffracted beams. (c) Geometry of moiré fringe formation. (d) Four principle stages of the tripod based preparation method of double lamella cross-sectional sample: 1. First surface (B) polishing parallel to zone axis [hkl]; 2. Second surface (C) polishing parallel to B; 3. Cutting into two pieces, 4. Two lamellas superposition.

changes, in the sample with the spatial resolution of the measurements limited to the moiré spacing. As we will show (see Methods), the corresponding lattice distortions can be conveniently extracted from moiré patterns by using the formalism of geometric phase analysis (GPA)<sup>18</sup>.

Happence has allowed moiré patterns to be investigated in different epitaxial samples, such as islands of InAs on GaAs<sup>21</sup>, Ge islands on Si<sup>22</sup> and YBa<sub>2</sub>Cu<sub>3</sub>O<sub>7</sub> thin film on MgO<sup>23</sup> where in plan-view the substrate is naturally superposed with the region of interest. The geometry is fixed and there can be no choice of orientation or fringe spacing. Here, we proposed two sample preparation methods that allow the formation of controlled moiré patterns, for more general structures, in cross-section and at specific sites. We will show how the spatial resolution of strain maps can be chosen as a function of the specimen preparation.

The principal technique is based on tripod specimen preparation (Fig. 1d). A cross-sectional lamella is prepared in the desired zone axis and carefully cut into two pieces that are put one upon the other. The upper lamella is displaced laterally until the substrate is superposed with the region of interest and rotated (if necessary). The art relies in precisely controlling the parallelism of the two adjacent surfaces during superimposition and the in-plane rotation angle that determines the spatial resolution of the technique. The possible disorientation of 0.05° between the two adjacent surfaces (see Methods) is one order of magnitude smaller than the values of typical Bragg angles varying in the range of 0.3–0.6°. Thus, the zone of interest can be considered as being in the same orientation as the reference lattice. A set of examples will illustrate the technique using a conventional TEM (a JEOL 2010 operating at 200 kV).

The first example consists of five fully relaxed Si<sub>1-x</sub>Ge<sub>x</sub> layers grown on top of a polished Si<sub>0.65</sub>Ge<sub>0.35</sub> virtual substrate<sup>24</sup>. This sample which has been characterized by X-ray diffraction (XRD) and Secondary Ion Mass

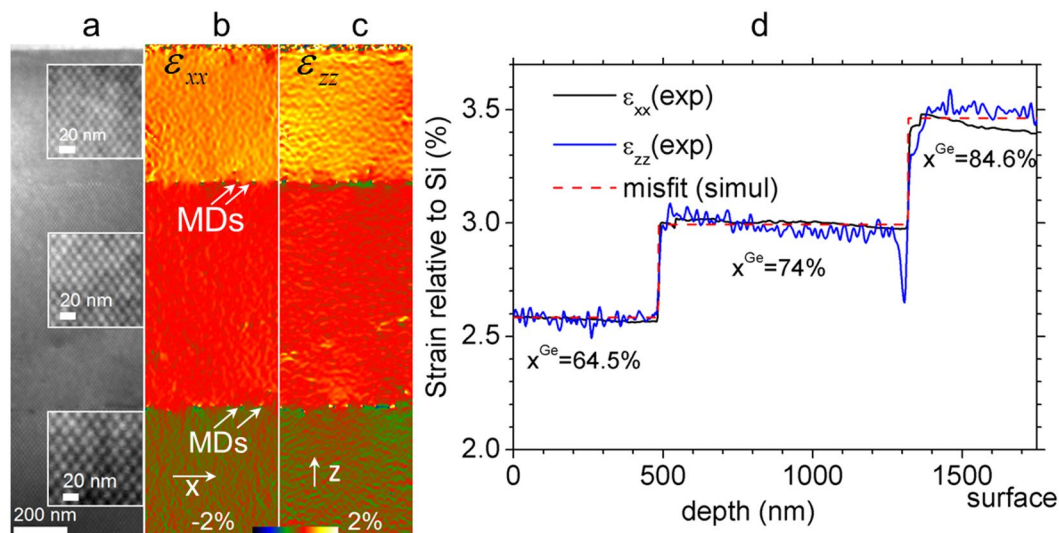


**Figure 2.** Structure consisting of five high Ge content completely relaxed  $\text{Si}_{1-x}\text{Ge}_x$  layers with  $x=45\%$ ,  $52\%$ ,  $64.5\%$ ,  $74\%$  and  $85\%$  grown on top of a polished  $\text{Si}_{0.65}\text{Ge}_{0.35}$  virtual substrate: **(a)** Bright-field cross-sectional (1–10) zone axis (ZA) [1–10] Moiré dot pattern formed over three upper layers (inserts show the zoomed parts of each layer) of a double lamella sample prepared with  $0^\circ$  rotation between two lamellas. **(b)** In-plane  $\epsilon_{xx}^{\text{Si}_{0.355}^{\text{e}}0.645}$  and **(c)** Out-of-plane  $\epsilon_{zz}^{\text{Si}_{0.355}^{\text{e}}0.645}$  strain maps. Misfit dislocations (MDs) are shown by arrows in **(b)**. **(d)** Experimental strain profiles (black and blue lines) and simulated misfit profile (red dashed line) calibrated with respect to Si.

Ge composition, $x$	Lattice parameter, $a^{\text{Si}_{1-x}\text{Ge}_x}$	Mismatch, $\delta$	Measurements	
			$\epsilon_{xx}$	$\epsilon_{zz}$
64.5%	0.5571 nm	2.58%	$2.57 \pm 0.09\%$	$2.57 \pm 0.11\%$
74.0%	0.5594 nm	3.00%	$2.99 \pm 0.06\%$	$2.96 \pm 0.08\%$
84.6%	0.5619 nm	3.46%	$3.42 \pm 0.07\%$	$3.49 \pm 0.12\%$

**Table 1.** Compilation of the results from the fully-relaxed  $\text{Si}_{1-x}\text{Ge}_x$  multilayers. Expected lattice parameters given by  $a^{\text{Si}_{1-x}\text{Ge}_x} = a^{\text{Si}} + 0.02005x + 0.00263x^2$  [29],  $a^{\text{Si}} = 0.5431 \text{ nm}$  and mismatch,  $\delta = (a^{\text{Si}_{1-x}\text{Ge}_x} - a^{\text{Si}})/a^{\text{Si}}$ . Measurements averaged over a 350 nm square area.

Spectroscopy (SIMS)<sup>25</sup> is ideal to show the accuracy and precision of the moiré-sample technique. In addition, the layers are already fully relaxed in the bulk sample, so there will be no thin-film relaxation in the TEM lamellas.

The moiré sample was prepared in (1–10) orientation, without any rotation between the two lamellas. A double moiré contrast is then formed by the interference of the two sets of (111) lattice planes of the Si substrate and the  $\text{Si}_{1-x}\text{Ge}_x$  layers (see insert in Fig. 2a). The geometric phase of the two sets of moiré fringes was determined and corrected for the projector lens distortions<sup>26</sup>. Given that the moiré fringe spacing was  $12.5 \pm 0.1 \text{ nm}$  in the bottom layer (the error is given by the magnification calibration accuracy of 1%), a spatial resolution of 25 nm was obtained for the strain analysis. The resulting strain (more precisely, deformation) maps give the difference between the local lattice parameter and the Si substrate in the x-direction parallel to the interface, and in the z-direction of growth (Fig. 2b and c respectively).

The layers being fully relaxed means that there should be no difference between the strain in the bulk sample and the TEM lamellas and the measurements are therefore directly comparable with X-ray data. Figure 2d shows vertical intensity profiles of  $\epsilon_{xx}$  (black line) and  $\epsilon_{zz}$  (blue line) averaged over a 400 nm distance along the interfaces which were recalibrated with respect to Si. The values of deformation measured both parallel and perpendicular to the layers,  $\epsilon_{xx}$  and  $\epsilon_{zz}$ , are in very good agreement with the previously determined misfit values (summarized in Table 1) for  $x=64.5\%$ ,  $74\%$  and  $84.6\%$ <sup>23</sup>. We can estimate the accuracy of the technique to be 0.02% and the precision from the standard deviation of the strain, to be as high as 0.01% for  $\epsilon_{xx}$  and 0.02% for  $\epsilon_{zz}$ .

This example shows that strain maps can be obtained over a huge field of view, 500 nm by 2 microns, which is very difficult to obtain with existing techniques, to very high precision and accuracy. Indeed, the accuracy is only limited by the calibration of the magnification since the moiré fringes measure the difference in lattice parameter between the substrate (upper lamella) and the area of interest (lower lamella). Unlike GPA or DFEH, no reference region is required as this has been already supplied by the substrate lamella. The precision is determined by the contrast of the moiré fringes. The spatial resolution (25 nm) is low but details in a vicinity of the interfaces reveal even the presence of misfit dislocations at the interfaces (white arrows in Fig. 2b). We will show in the next example how the spatial resolution of the moiré sample technique can be adjusted to even nanometer resolution by applying controlled sample rotations during preparation.

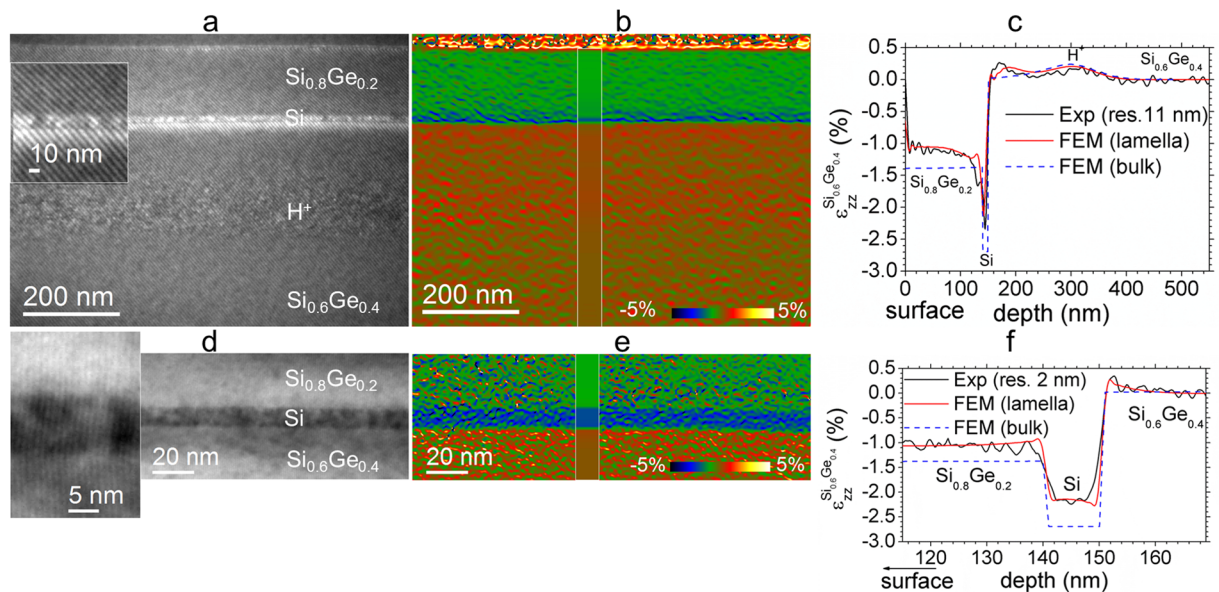


**Figure 3.** Structure consisting of a  $\text{Si}_{1-x}\text{Ge}_x$  virtual substrate capped by a thick, constant composition completely relaxed  $\text{Si}_{0.6}\text{Ge}_{0.4}$ /10 nm-thick Si/170 nm-thick  $\text{Si}_{0.8}\text{Ge}_{0.2}$  layers implanted by  $\text{H}^+$  ions. Cross-sectional (1–10) double lamella samples with (a–c),  $3.2^\circ$  (sample ‘A’) and (d–f)  $7.8^\circ$  (sample ‘B’) rotation between lamellas: dark-field single moiré fringe images taken with a,  $g = 111$  and d,  $g = 004$ . (b,e) Corresponding out-of-plane  $\varepsilon_{zz}^{\text{Si}_{0.6}\text{Ge}_{0.4}}$  experimental strain maps with simulated strain maps inserted. (c,f), Line profiles: experimental strain profiles (black lines), FEM simulated in a TEM lamella (red lines) and in bulk (blue dashed lines).

The example structure consists of a  $\text{Si}_{1-x}\text{Ge}_x$  virtual substrate capped by a thick, constant composition completely relaxed  $\text{Si}_{0.6}\text{Ge}_{0.4}$ /10 nm-thick Si/170 nm-thick  $\text{Si}_{0.8}\text{Ge}_{0.2}$  layers implanted by  $\text{H}^+$  ions (see Methods). Two different moiré samples ‘A’ and ‘B’ were prepared in (1–10) cross-section, overlapping the Si substrate with the region of interest, as before, but this time with applying rotations of  $3.2^\circ$  (sample ‘A’) and  $7.8^\circ$  (sample ‘B’) between the upper and lower lamellas. Figure 3a–c show a dark-field moiré image taken with  $g = 111$ , out-of-plane strain map extracted with a spatial resolution of 11 nm and corresponding strain profile (black line) of the sample ‘A’. Whilst a spatial resolution of 11 nm is good enough for mapping strain in thick  $\text{Si}_{1-x}\text{Ge}_x$  layers over a large field of view, it blurs the strain profile in the thin Si layer.

Figure 3d shows a DF image of the second sample taken with  $g = 004$  demonstrating a Moiré pattern consisting of one set of fringes (zoomed part around the Si layer is shown in insert) with a period of only 1 nm. The map of  $\varepsilon_{zz}$  (Fig. 3e) was extracted with a 2 nm spatial resolution revealing the details of the strain in thin Si layer clearly.

Thin-film relaxation is significant in this sample, so FEM modelling was carried out assuming a foil thickness of 30 nm (see Methods). The deformation is reduced by about 22% with respect the values in a bulk structure (Fig. 3f, blue dashed line). The excellent agreement with the experimental profiles suggests that an accuracy and precision of 0.1% can be reached even at such ultimate spatial resolution of 2 nm.

The tripod method is well efficient for mapping inhomogeneous strain fields associated to 3D objects such as quantum dots (Fig. 4a,c,e) in excellent quantitative agreement with 3D FEM simulations (Fig. 4b,d,f). However, devices usually require a site-specific method of preparation. For this reason, we have also developed a moiré-sample preparation method with the FIB (Fig. 5).

The rotation angle, and tilt, between the two lamellas is much more difficult to control in the FIB than for the conventional specimen preparation. For example, only one set of moiré fringes were available for each sample and the fringe spacing, notably for the (004) lattice planes, could have been finer. Nevertheless, this example shows that FIB preparation is a possibility to explore for strain mapping where site specificity is necessary. We believe that a further development of the FIB method would allow to superimpose lamellas with a controlled angle of rotation and, thus, to reach a nanometer resolution for strain mapping.

Strain measurements by specimen design are not only comparable with existing techniques but can be obtained for fields of view only limited by the sample dimensions. Strain is also measured with respect to a well-defined reference ensuring high accuracy. We anticipate that the principle of specimen design can be extended to other types of measurement and to other types of epitaxial samples such as ferroelectric oxides, metals and ceramics.

## Methods

**Sample preparation.** The growth of the fully relaxed  $\text{Si}_{1-x}\text{Ge}_x$  layers is fully described in<sup>24</sup>, the  $\text{Si}_{1-x}\text{Ge}_x$  quantum dots in<sup>27</sup>, and the MOSFET devices in<sup>28</sup>. The  $\text{H}^+$  implanted structure consisted of the following layers grown by CVD on a  $\text{Si}_{1-x}\text{Ge}_x$  virtual substrate: a thick layer of completely relaxed  $\text{Si}_{0.6}\text{Ge}_{0.4}$ , 10 nm-thick in-plane tensile strained Si, and 170 nm-thick in-plane tensile strained  $\text{Si}_{0.8}\text{Ge}_{0.2}$  layer. The sample was then implanted by  $\text{H}^+$  ions at 30 keV to a fluence of  $1 \times 10^{16} \text{ cm}^{-2}$  in the same way as for the silicon sample described in<sup>29</sup>.

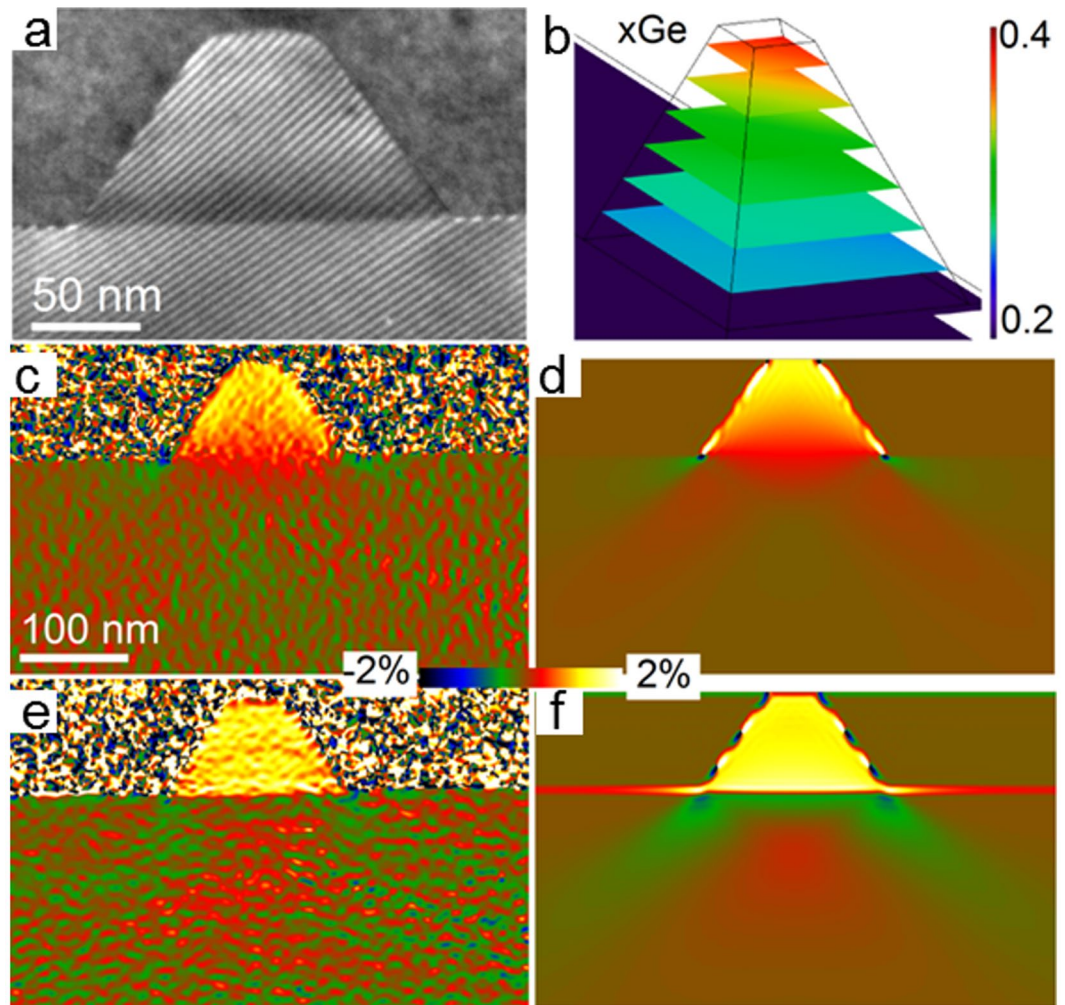


**Figure 4.** Moiré analysis of coherently strained SiGe quantum dot on Si substrate: (a) (111) moiré fringes. (b) Modelled germanium concentration. (c,e) Measured strain component parallel and perpendicular to interface, respectively. (d,f) Corresponding strain maps from finite element analysis.

**Moiré sample preparation.** The four principle stages of the tripod preparation method are (Fig. 1d): (1) gluing of a cross-sectional sample, cutting a slice, tripod based grinding of the slice butt (A), grinding and polishing of the slice front side (B); (2) grinding and polishing of the slice back side (C) leaving a 300  $\mu\text{m}$ –600  $\mu\text{m}$ -thick lamella with mutually parallel B and C surfaces. Both surfaces B and C should be approximately perpendicular to the desired direction of the sample observation [hkl] (marked as zone axis (ZA) [hkl]). Polishing is realized on a felt using a colloidal solution of the silica grains to atomically smooth surfaces B and C; (3) cutting of the slice into 2 quasi-equivalent pieces I and II; (4) superposition of two pieces in a manner that: the surface C of part II is face to face with respect to surface B of part I; the surface A' of part I is above the surface A of part II; part I is displaced at a distance of 400–600  $\mu\text{m}$  from the boards of part II; part I is rotated with respect to part II at the desired angle (between 0–15°) in the plane of surface B. The surfaces B and C become parallel when the polished slice gets the same thickness over its whole length and width. The thickness of the slice is controlled in an optical microscope with a  $\pm 5 \mu\text{m}$  precision. For a 6 mm long slice, such thickness variation corresponds to about 0.05° disorientation between the surfaces B and C.

The sample is put in a press, epoxy glue applied around the edges, and then into an oven at 80 °C. The mechanical pressure and the epoxy glue are necessary to have a good contact between the surfaces, to minimize the distance between them, if any, and to immobilise the configuration. Both parts I and II of the double lamella are then thinned by tripod grinding down to a thickness of 10  $\mu\text{m}$ . The final stage comprised of Ar<sup>+</sup> ion-beam thinning on both sides of the sample with a PIPS (Gatan) until electron transparency is obtained. As a result, the zones of interest in part II are covered by the substrate (part I) consisting of known and undistorted material (red zone, step 4) or vice versa (blue zone, step 4).

The FIB samples (Fig. 5) were prepared using a Helios FIB-SEM (FEI). A standard extraction procedure was first carried out as follows. A 200 nm thick Pt layer was deposited with electron beam assistance to protect the sample surface, followed by ion-beam deposition of a thick 3  $\mu\text{m}$  layer of Pt. Trenches were milled on both sides of the deposit. A piece of sample was then cut and lifted out using a nano-manipulator (Omniprobe). The piece

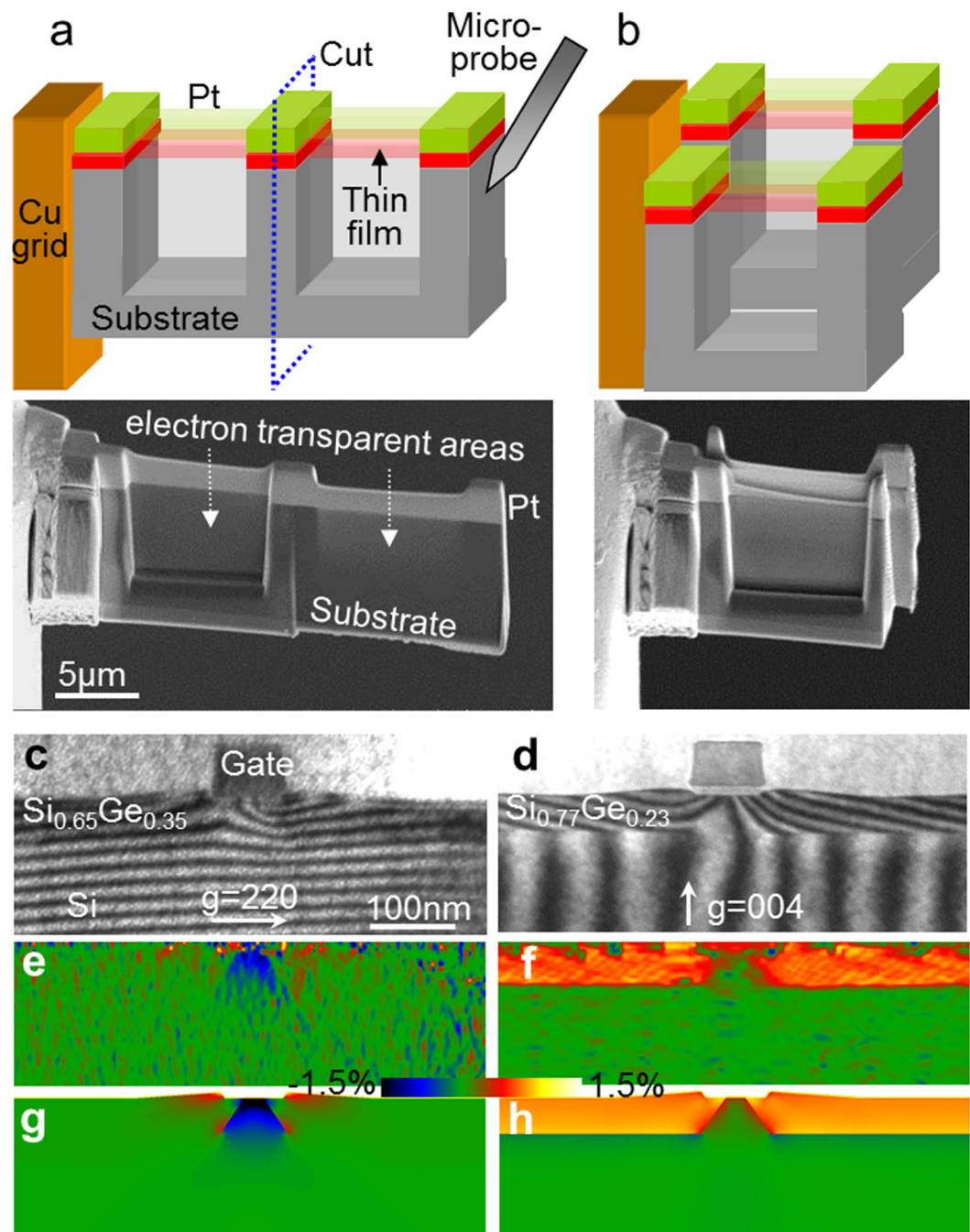


**Figure 5.** (a,b) Principle stages of the FIB based preparation method of double lamella cross-sectional sample: (a) Schematic representation and SEM image of an epitaxial sample prepared by focused ion beam. A piece of sample was cut from the bulk, lifted-out and attached to a grid. Two windows were thinned to electron transparency. (b) Schematic representation and SEM image of the finished double lamella sample. Right window in (a) was freed and moved behind the left one using a micro-probe. It was shifted of a few microns in the vertical direction such a way that its substrate overlaps the epitaxial thin film of the fixed window. (c–h) Site-specific moiré analysis of strained-silicon transistor: (c,d) Moiré fringes of two similar transistors for (220) and (004) lattice planes, respectively. (e,f) Measured strain components, respectively parallel and perpendicular to interface. (g,h) Corresponding strain maps from finite element analysis.

was attached to a grid using Pt deposition and thinned down to about 500 nm at 30 kV. Two 8 µm wide windows were then thinned to electron transparency (Fig. 5a,b) at 8 kV to reduce the amorphization of the surfaces. A tilt of  $\pm 2^\circ$  was applied to compensate for the Gaussian shape of the ion beam.

The probe was then attached again to the free side of the sample and the two windows were separated (Fig. 5c). The detached window was positioned behind the other one and shifted a few microns in the vertical direction, in such a way that its substrate overlaps the epitaxial thin film of the fixed window. For the last steps, care should be

taken to avoid imaging the lamellae in order to avoid re-deposition of Pt on the surfaces. Since the alignment of the lamellas with the micro-probe is never perfect, small rotations occur when detaching/attaching the lamella. The rotation angle between the two lamellas is typically less than 1° which corresponds to a moiré period greater than 20 nm.

**TEM observations.** The moiré samples prepared by tripod polishing were observed on a Jeol 2010 TEM with a LaB<sub>6</sub> gun operating at 200 kV. Images were acquired on a CDD camera (1376 × 1032 pixels) using 1 to 5 s acquisition times. The FIB-prepared samples were observed on a Philips CM20FEG microscope, equipped with a Schottky field emission gun operated at 200 kV. Images were acquired on a CCD camera (2k by 2k pixels binned by 2) using 5 to 10 s acquisition times.

**Moiré analysis.** Moiré patterns were analyzed using modified version of HoloDark 1.0 (HREM Research, Inc.), plugin for the image processing software Digital Micrograph (Gatan Inc.). The phase of the moiré fringes was assumed to be equal to the geometric phase of the diffracted beams forming the moiré pattern and the strain maps calculated accordingly. The geometric phase was corrected for the projector lens distortions<sup>26</sup>. The spatial resolution for the strain measurements was defined by the radius of the mask used for inverse Fourier reconstruction and was, at best, twice the moiré period.

For the reconstruction of the geometric phase for the FIB-prepared samples, where the fringe spacing is large, we used a reconstruction method functioning in real space<sup>30</sup> which allows the improvement of the spatial resolution by a factor of 2 with respect to the Fourier method used in GPA<sup>6</sup> or DFEH<sup>11</sup>. It involves several steps: detection of the fringe minimums and maximums, calculation of envelope functions, normalization of the interference pattern to retrieve the cosine function and finally calculation of the phase image.

**Modeling.** Finite element method (FEM) modeling was performed using the structural mechanics module of COMSOL Multiphysics. The samples were simulated in 2D (when appropriate) and 3D, taking into account the elastic relaxation at the free surfaces of the thin foil. Mismatch between epitaxial layers was incorporated in the usual way as an initial deformation. The deformation and displacement fields were averaged over the thickness of the lamella using a weighting function<sup>31,32</sup> and imported into Digital Micrograph (Gatan Inc.). Moiré patterns and phase images were then calculated from the simulated displacement field and treated exactly as the experimental images. The foil thickness was measured using the extinction fringes of {111} reflection of the crystal in dark-field TEM imaging.

The modeling of the H<sup>+</sup> ions implanted sample required a specific treatment, as described in<sup>29,33</sup> for a silicon sample implanted with H<sup>+</sup> ions under similar conditions. First the H profile,  $c_H(z)$ , as a function of the depth,  $z$ , was determined by SRIM code<sup>34</sup>. The misfit was described analytically as  $\varepsilon_{xx}(z) \cong -0.17c_H(z)$ . A weighting function was calculated for a TEM lamella thickness of 100 nm,  $g = 111$ , deviation from exact Bragg conditions  $s = 0.012 \text{ nm}^{-1}$ .

For the quantum dot sample, the Ge composition distribution within the island was modeled in the same way as for a pyramid-shaped InGaAs/GaAs quantum dot<sup>35</sup> but modified for a 45° rotation of the pyramid square base (Fig. 4b). The concentration of Ge in the pyramid of height,  $H$ , and base length,  $L$ , is described by  $c(x, y, z) = c_{base} + \frac{Lz(c_{facet}(z) - c_{base})}{H(L - x - y)}$  where the origin (0,0,0) is situated at the center of the island base and the Ge distribution along the facets is given by  $c_{facet}(z) = c_{facetbase} + (c_{apex} - c_{facetbase})\sqrt{z/H_{pyr}}$ . The constants  $c_{base} = 0.23$ ,  $c_{facetbase} = 0.15$  and  $c_{apex} = 0.39$  stand for the Ge concentration in the base of the object and the facets for  $z = 0$  and for the Ge concentration in the apex of the full pyramid for  $z = H_{pyr}$ .

## References

- Lee, M. L. *et al.* Strained Si, SiGe, and Ge channels for high-mobility metal-oxide-semiconductor field-effect transistors. *J. Appl. Phys.* **97**, 011101 (2005).
- Schlom, D. G. *et al.* Strain tuning of ferroelectric thin films. *Annual Review of Materials Research* **37**, 589–626 (2007).
- Biswas, K. *et al.* Strained endotaxial nanostructures with high thermoelectric figure of merit. *Nature Chemistry* **3**, 160–166 (2011).
- Hýtch, M. J. & Minor, A. Observing and measuring strain in nanostructures and devices with transmission electron microscopy. *MRS Bulletin* **39**, 138–146 (2014).
- Bierwolf, R. *et al.* Direct measurement of local lattice distortions in strained layer structures by HREM. *Ultramicroscopy* **49**, 273 (1993).
- Hýtch, M. J., Snoeck, E. & Kilaas, R. Quantitative measurement of displacement and strain fields from HREM micrographs. *Ultramicroscopy* **74**, 131 (1998).
- Frabboni, S. *et al.* Lattice strain and static disorder determination in Si/Si<sub>1-x</sub>Ge<sub>x</sub>/Si heterostructures by convergent beam electron diffraction. *Phys. Rev. B* **60**, 13750 (1999).
- Hýtch, M. J., Putaux, J.-L. & Pénisson, J.-M. Measurement of the displacement field around dislocations to 0.03 Å by electron microscopy. *Nature* **423**, 270–273 (2003).
- Usuda, K., Numata, T., Irisawa, T., Hirashita, N. & Takagi, S. Strain characterization in SOI and strained-Si on SGOI MOSFET channel using nano-beam electron diffraction (NBD). *Mater. Sci. Eng. B* **124**, 143–147 (2005).
- Cooper, D., Bernier, N. & Rouvière, J. L. Combining 2 nm Spatial Resolution and 0.02% Precision for Deformation Mapping of Semiconductor Specimens in a Transmission Electron Microscope by Precession Electron Diffraction. *Nano Letters* **15**, 5289–5294 (2015).
- Hýtch, M. J., Houdellier, F., Hüe, F. & Snoeck, E. Nanoscale holographic interferometry for strain measurements in electronic devices. *Nature* **453**, 1086 (2008).
- Koch, C. & Lubk, A. Off-axis and inline electron holography: A quantitative comparison. *Ultramicroscopy* **110**(5), 460–471 (2010).
- Koch, C. *et al.* An efficient, simple, and precise way to map strain with nanometer resolution in semiconductor devices. *Appl. Phys. Lett.* **96**, 091901 (2010).
- Su, D. & Zhu, Y. M. Scanning moiré fringe imaging by scanning transmission electron microscopy. *Ultramicroscopy* **110**, 229–233 (2010).



15. Kim, S. *et al.* Scanning moiré fringe imaging for quantitative strain mapping in semiconductor devices. *Applied Physics Letters* **102**, 161604 (2013).
16. Clément, L., Pantel, R., Kwakman, L. F. T. & Rouvière, J.-L. Strain measurements by convergent-beam electron diffraction: The importance of stress relaxation in lamella preparations. *Appl. Phys. Lett.* **85**, 651–653 (2004).
17. Houdellier, F., Roucau, C., Clément, L., Rouvière, J.-L. & Casanove, M.-J. Quantitative analysis of HOLZ line splitting in CBED patterns of epitaxially strained layers. *Ultramicroscopy* **106**, 951–959 (2006).
18. Menter, J. W. The Direct Study by Electron Microscopy of Crystal Lattices and their Imperfections. *Proc. Roy. Soc. London. Series A. Mathematical and Physical Sciences* **236**, 119 (1956).
19. Bassett, G. A., Menter, J. W. & Pashley, D. W. Moiré Patterns on Electron Micrographs, and their Application to the Study of Dislocations in Metals. *Proc. Roy. Soc. London A: Mathematical, Physical and Engineering Sciences* **246**, 345 (1958).
20. Lord Rayleigh (Strutt J.W.). On the manufacture and theory of diffraction-gratings. *Phil. Mag.* **47**, 193–205 (1874).
21. Androussi, Y., Benabbas, T. & Lefebvre, A. Moiré-like fringes in transmission electron microscopy images of coherently strained semiconductor islands. *Ultramicroscopy* **93**, 161 (2002).
22. Hiroyama, Y. & Tamura, M. *In situ* observations of nucleation and coalescence stages in Ge growth on Si surfaces using transmission electron microscope combined with molecular beam epitaxy chamber. *J. Vac. Sci. Technol. A* **16**, 2956 (1998).
23. Norton, M. G. & Carter, C. B. Moiré patterns and their application to the study of the growth of  $\text{YB}_2\text{C}_6\text{O}_{7-8}$  thin films. *J. Mat. Sci.* **30**, 381 (1995).
24. Hartmann, J. M., Baud, L., Rolland, G., Fabbri, J. M. & Billon, T. Very High Temperature Growth of SiGe Virtual Substrates ( $15\% < [\text{Ge}] < 45\%$ ). *ECS Trans.* **3**, 219 (2006).
25. Gavelle, M. *et al.* Detection of  $\text{Cs}_2\text{Ge}^+$  clusters for the quantification of germanium atoms by secondary ion mass spectrometry: Application to the characterization of  $\text{Si}_{1-x}\text{Ge}_x$  layers ( $0 \leq x \leq 1$ ) and germanium diffusion in silicon. *J. of Appl. Phys.* **102**, 074904 (2007).
26. Hüe, F. *et al.* Calibration of projector lens distortions. *J. Electron Microsc. (Tokyo)* **54**, 181–190 (2005).
27. Groenen, J. *et al.* Phonons as probes in self-organized SiGe islands. *Appl. Phys. Lett.* **71**, 3856 (1997).
28. Hartmann, J. M. *et al.* Low temperature boron and phosphorous doped SiGe for recessed and raised sources and drains. *J. Cryst. Growth* **327**, 68–77 (2011).
29. Cherkashin, N., Reboh, S., Lubk, A., Hÿtch, M. J. & Claverie, A. Strain in Hydrogen-Implanted Si Investigated Using Dark-Field Electron Holography. *Appl. Phys. Expr.* **6**, 091301 (2013).
30. Fujita, T., Yamamoto, K., McCartney, M. R. & Smith, D. J. Reconstruction technique for off-axis electron holography using coarse fringes. *Ultramicroscopy* **106**, 486 (2006).
31. Lubk, A. *et al.* Dynamic scattering theory for dark-field electron holography of 3D strain fields. *Ultramicroscopy* **136**, 42 (2014).
32. Javon, E. *et al.* Dynamical effects in strain measurements by dark-field electron holography. *Ultramicroscopy* **147**, 70 (2014).
33. Cherkashin, N. *et al.* Modelling of point defect complex formation and its application to  $\text{H}^+$  ion implanted silicon. *Acta Materialia* **99**, 187 (2015).
34. Ziegler, J. F., Biersack, J. P. SRIM computer code <http://www.srim.org>.
35. Cherkashin, N. *et al.* Determination of stress, strain, and elemental distribution within In(Ga)As quantum dots embedded in GaAs using advanced transmission electron microscopy. *Appl. Phys. Lett.* **102**, 173115 (2013).

## Acknowledgements

N.C. and M.H. thank European Union Seventh Framework Program (FP7/2007–2013) under grant agreement N. 318388 for financial support. This work has been supported by the French National Research Agency under the “Investissement d’Avenir” program reference No. ANR-10-EQPX-38-01”. We thank J.M. Hartmann and J. Groenen for providing the materials.

## Author Contributions

N.C. proposed the idea, conceived and realized the experiment related to tripod based double lamella sample preparation and absolute strain measurements. T.D. conceived and realized the experiment related to F.I.B. based double lamella sample preparation and carried out FEM modelling. N.C. and M.J.H. carried out the analysis and wrote the paper. All authors discussed the results.

## Additional Information

**Competing Interests:** The authors declare that they have no competing interests.

**Publisher's note:** Springer Nature remains neutral with regard to jurisdictional claims in published maps and institutional affiliations.



**Open Access** This article is licensed under a Creative Commons Attribution 4.0 International License, which permits use, sharing, adaptation, distribution and reproduction in any medium or format, as long as you give appropriate credit to the original author(s) and the source, provide a link to the Creative Commons license, and indicate if changes were made. The images or other third party material in this article are included in the article's Creative Commons license, unless indicated otherwise in a credit line to the material. If material is not included in the article's Creative Commons license and your intended use is not permitted by statutory regulation or exceeds the permitted use, you will need to obtain permission directly from the copyright holder. To view a copy of this license, visit <http://creativecommons.org/licenses/by/4.0/>.

© The Author(s) 2017